REPORT DOCUMENTATION PAGE

Public reporting burden for this collection of information is estimated to average 1 hour per response, including the time for reviewing instructions, searching existing data sources, gathering and maintaining the data needed, and completing and reviewing this collection of information. Send comments regarding this burden estimate or any other aspect of this collection of information, including suggestions for reducing this burden to Department of Defense, Washington Headquarters Services, Directorate for Information Operations and Reports (0704-0188), 1215 Jefferson Davis Highway, Suite 1204, Arlington, VA 22202-4302. Respondents should be aware that notwithstanding any other provision of law, no person shall be subject to any penalty for failing to comply with a collection of information if it does not display a currently valid OMB control number. **PLEASE DO NOT RETURN YOUR FORM TO THE ABOVE ADDRESS.**

1. REPORT DATE (DD-MM-YYYY) 30-05-2008	2. REPORT TYPE Technical Paper	3. DATES COVERED (From - To)

4. TITLE AND SUBTITLE

Analysis of Physical and Numerical Factors for Prediction of UV Radiation from High Altitude Two-Phase Plumes (Preprint)

5a. CONTRACT NUMBER

5b. GRANT NUMBER

5c. PROGRAM ELEMENT NUMBER

6. AUTHOR(S)

Natalia E. Gimelshein, Robert B. Lyons, & James G. Reuster (EC); Sergey F. Gimelshein (USC)

5d. PROJECT NUMBER

5e. TASK NUMBER

5f. WORK UNIT NUMBER
MDA0086P

7. PERFORMING ORGANIZATION NAME(S) AND ADDRESS(ES)

Air Force Research Laboratory (AFMC)
AFRL/RZSA
10 E. Saturn Blvd.
Edwards AFB CA 93524-7680

8. PERFORMING ORGANIZATION REPORT NUMBER

AFRL-RZ-ED-TP-2008-188

9. SPONSORING / MONITORING AGENCY NAME(S) AND ADDRESS(ES)

Air Force Research Laboratory (AFMC)
AFRL/RZS
5 Pollux Drive
Edwards AFB CA 93524-7048

10. SPONSOR/MONITOR'S ACRONYM(S)

11. SPONSOR/MONITOR'S NUMBER(S)

AFRL-RZ-ED-TP-2008-188

12. DISTRIBUTION / AVAILABILITY STATEMENT

Approved for public release; distribution unlimited (PA #08224A).

13. SUPPLEMENTARY NOTES
Submitted for presentation at the 40th AIAA Thermophysics Conference, to be held in Seattle, WA, 23-26 June 2008.

14. ABSTRACT

Numerical study of a 5,900 lb solid propellant thruster plume at an altitude of 118 km is performed using a combined multi-step continuum/kinetic approach. The Navier-Stokes equations are solved for the flow inside the nozzle and the first several meters into the plume. The DSMC method is used to simulate the remaining plume and the plume-free stream interaction. A Monte Carlo based radiation code is applied in an overlay mode to calculate UV radiation in the near and far field of the plume. The computations take into account both alumina particles and soot. The effect of alumina particle emissivities and size distribution, as well as soot concentration, on UV radiation is clarified. Comparison of numerical results with available UV measurements is conducted.

15. SUBJECT TERMS

16. SECURITY CLASSIFICATION OF:			17. LIMITATION OF ABSTRACT	18. NUMBER OF PAGES	19a. NAME OF RESPONSIBLE PERSON Mr. Thomas Smith
a. REPORT Unclassified	b. ABSTRACT Unclassified	c. THIS PAGE Unclassified	SAR	18	19b. TELEPHONE NUMBER (include area code) N/A

Analysis of Physical and Numerical Factors
for Prediction of UV Radiation from
High Altitude Two-Phase Plumes (Preprint)

Natalia E. Gimelshein,*
Robert B. Lyons,†
and James G. Reuster†

ERC, Inc., Edwards AFB, CA 93524

Sergey F. Gimelshein‡

USC, Los Angeles, CA 90089

Numerical study of a 5,900 lb solid propellant thruster plume at an altitude of 118 km is performed using a combined multi-step continuum/kinetic approach. The Navier-Stokes equations are solved for the flow inside the nozzle and the first several meters into the plume. The DSMC method is used to simulate the remaining plume and the plume-free stream interaction. A Monte Carlo based radiation code is applied in an overlay mode to calculate UV radiation in the near and far field of the plume. The computations take into account both alumina particles and soot. The effect of alumina particle emissivities and size distribution, as well as soot concentration, on UV radiation is clarified. Comparison of numerical results with available UV measurements is conducted.

I.   Introduction

The success of missile signature analysis depends heavily on the reliability of signature predictions for all stages of the boost trajectory. Prediction reliability, in turn, is significantly hampered by a large number of uncertainties and unknowns currently associated with the physics and gas dynamics of rocket propulsion system exhaust plumes interacting with the surrounding atmosphere. An essential feature of solid propellant rocket plumes that complicates flow analysis is related to the formation of particulates of varying types, sizes, and loadings. This makes rocket plume flows two-phase, with one phase consisting of gas atoms and molecules and the other composed of nano- and micro-scale particulates. Disregard of the two-phase character of rocket plumes usually results in unacceptable loss in prediction accuracy. The specifics of interaction between the two phases and its impact on signatures and contamination depends on the propellant composition and thruster operation. The main particulate types are soot, propellant droplets, and aluminum oxide particles. The large particle phase mass fractions of the latter have a significant impact on the gas flow inside the nozzle (and therefore thruster performance), the near field plume structure, and the far field plume-atmosphere interaction structure. The strong influence from these particles on the flow structure inside the nozzle and in the plume results in a dramatic effect on radiation signatures.

There are a number of physical processes and quantities that affect radiation from rocket plumes in the UV region, most are associated with various particulate properties and propellant/motor parameters. In the related previous work,[1] one of these processes was considered in detail, namely photon scattering on alumina particles in a Star-27 motor plume at 118 km. The numerical results were compared with available on-board flight measurements[2] for two lines of sight; near field (4° from the plume axis) and far field (25°). It was shown that the main process determining the far field radiation is photon scattering on submicron particles. Accounting for this effect increases the predicted radiance by a factor of 300, and the value of the full radiance at 230 nm in this case was approximately a factor of four lower than the measurements. The

---

*Consultant
†Senior Aerospace Engineer, Propulsion Directorate
‡Research Assistant Professor, Department of Aerospace and Mechanical Engineering.

predicted near field radiation was only about 30% higher than the measurements at 230 nm. This difference increases to an order of magnitude at 400 nm.

The main goal of this work, that is a continuation of Ref. 1, is to analyze possible reasons for the difference between computed and experimental results, at both inband and spectral levels. Similar to Ref. 1, a multi-step continuum-kinetic approach is used. Continuum Navier-Stokes solvers VIPER and CFD++ are used to predict the flow inside of the nozzle and in the near field of the plume, respectively. A kinetic DSMC-based solver SMILE is used in the mid- and far fields of the flow. The final flow solution is obtained through successive application of these solvers from the inside the nozzle to the outside, with the information transferred through boundary conditions (starting surfaces). Finally, a Monte Carlo radiation code NEMO is applied to calculate UV radiation.

The following important factors are examined.

(i) **The impact of soot particles on spectra in the far field.** Soot particles, common to both hydrocarbon and solid propellant systems,[4] do not significantly affect the plume gas flow due to their small concentrations, but are of interest due to their possible influence on radiation signatures. Soot particles are included in the present simulations in addition to the alumina particles considered previously, and the effect of their loading and size distribution is clarified below. Another possible source of small particulates in the plume, related to the homogeneous and heterogeneous condensation processes, is not considered in this work.

(ii) **Alumina particle emissivities.** There are a number of particle material properties that may potentially impact the gas and particle parameters in the plume. One of the most important properties related to radiation signatures is particle emissivity. Particle emissivity can be accurately calculated for spherical particles using Mie theory, provided the complex index of refraction is defined as a function of temperature and wavelength. Comparison of the complex index of refraction deduced from available experimental data shows difference of up to two orders of magnitude observed between different experiments. Since the real part of the refraction index is nearly constant and much larger than the imaginary part, this two orders of magnitude difference in the imaginary part translates to two orders of magnitude difference in particle emissivities. In the present work, existing theoretical and empirical correlations for the particle refraction index are analyzed, and the sensitivity of radiation signatures from a Star 27 motor to particle emissivities are examined.

(iii) **Alumina particle size distribution.** Experimental evidence[3] indicates the presence of a substantial number of submicron particles in solid propellant rocket plumes. The size distribution of submicron particles exhibits substantial variability for different motor designs.[3, 4] A submicron particle size distribution for the Star-27 motor has not been measured to the authors' knowledge, so three models were developed to test the sensitivity of UV emissions to the assumed size distribution. The three distributions span four orders of magnitude in assumed mass fraction for 0.2 micron diameter particles. This range of particle sizes tests the importance of small aluina particle scattering on the 25° model data comparisons.

II. Flow Conditions

Availability of detailed in-flight measurements of UV radiation from second and third stage plumes of the Strypi XI rocket provides a solid basis for numerical model testing and validation.[6] These measurements were conducted during the Bow Shock Ultraviolet 2 Experiment flown in early 1991. As part of this experiment, inband and spectrally resolved radiation from the Antares II motor (second stage) and the Star 27 motor (third stage) in the range from 200 to 400 nm were recorded for flight altitudes from approximately 104 km to 119 km. For data collection, aft-viewing photometers and spectrometers installed on extractable periscopes were used. Two lines of sight were examined, 4 deg and 25 deg from the rocket centerline.

In this work, the point of the flight trajectory that has been numerically examined corresponds to the Star 27 steady state operation at an altitude of 118 km. The geometric setup used to approximate experimental conditions is shown in Fig. 1a. The free stream temperature and density are 330 K and 5.21×10^{17} molecule/m^3, and the atmosphere species mole fractions are 66.7% N_2, 7.6% O_2, and 25.7% O. The rocket moves with velocity of 2850 m/s. Zero angle of attack was assumed in the computations. The nozzle thrust is about 5,900 lb. The exhaust gas composition is listed in Table 1.

Three alumina particle size distributions are considered in this work, all of them assuming the total mass fraction of the alumina particles in the exhaust of 29.5%. The first distribution is a 5-particle bin distribution used in the previous work,[1] and shown in Table 2. The second distribution is based on the Worster[5] particle size model. The Worster distribution produced the smallest mass fractions for the submicron particles (see

American Institute of Aeronautics and Astronautics Paper 2008-4120
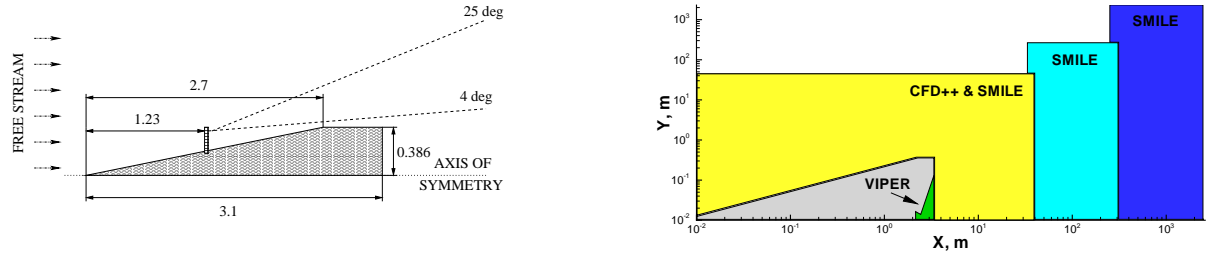
Figure 1. Schematics of the geometrical setup (left) and the computational domains used in the present multi-step approach (right).

Table 1. Mole Fractions (M.F.) of major plume species.

Species	CO	CO_2	Cl	H	H_2	H_2O	HCl	OH	N_2
M.F.	0.2225	0.0291	8.67×10^{-3}	0.0190	0.2734	0.1767	0.1590	5.38×10^{-4}	0.1108

Table 3). A larger mass fraction of submicron particles is used in the third, 14-particle bin, distribution, presented in Table 4. The alumina particle mass fractions for these three distributions are illustrated in Fig. 2.

Two different mass fractions of soot particles were considered, 0.3 and 3% of the total propellant mass. The distribution of soot particle sizes was represented by three bins, 40, 100, and 200 nm. All bins are assumed to have $\frac{1}{3}$ of the total soot mass fraction. This soot size distribution was used for all three alumina particle size distribution cases.

Table 2. 5-bin distribution of alumina particles at the nozzle exit.

Bin #	1	2	3	4	5
Diameter, μm	0.2	3.66	6.11	8.54	11.0
Mass fraction	0.15	0.43	0.29	0.10	0.03

III.   Numerical Approaches

A.   Multi-Step Numerical Approach

Modeling of a rocket plume expanding into a high altitude atmosphere is a numerically challenging problem, primarily due to the large variation in gas density and spatial scales. The flow regime varies from continuum inside the nozzle, to transitional in the near field, to free molecular in the far field of the plume. The scales of interest vary from centimeters inside the nozzle to kilometers in the plume. The change in flow regime makes application of a single numerical approach very difficult. Continuum approaches, such as those based on the solution of Navier-Stokes equations, cannot be applied to describe nonequilibrium flows in the far field of the plume. On the other hand, the use of kinetic approaches, such as direct simulation Monte Carlo (DSMC) method, to predict continuum flow inside the nozzle, although theoretically possible, is prohibitively expensive from a computational standpoint. The factor that simplifies numerical analysis is that the plume flow is typically supersonic, which means that the upstream influence of any specific point in the plume is minimal. Therefore it is both reasonable and convenient to apply a combined continuum-kinetic technique, with the continuum part of the flow being modeled by a Navier-Stokes solver, and the transitional flow computed by a kinetic method. In this work, the following combined multi-step technique, schematically illustrated in Fig. 1b, has been used.

Step 1: **flow inside the nozzle.** A continuum method is applied to calculate the flow inside the nozzle. The solution of the parabolized Navier-Stokes equations on a structured grid is obtained with the VIPER

Table 3. 15-bin distribution of alumina particles at the nozzle exit.

Bin #	1	2	3	4	5	6	7	8
Diameter, μm	0.075	0.2	0.3	0.4	0.5	0.6	0.7	0.8
Mass fraction	8.64e-6	5.38e-5	1.62e-4	3.51e-4	6.29e-4	9.98e-4	1.5e-3	2e-3

Bin #	9	10	11	12	13	14	15
Diameter, μm	0.9	1	1.74	3.66	6.1	8.54	11
Mass fraction	2.6e-3	3.3e-3	0.113	0.423	0.282	0.11	0.04

Table 4. 14-bin distribution of alumina particles at the nozzle exit.

Bin #	1	2	3	4	5	6	7
Diameter, μm	0.075	0.2	0.3	0.4	0.5	0.6	0.7
Mass fraction	0.0207	0.0216	0.0190	0.0168	0.0150	0.0136	0.0123

Bin #	8	9	10	11	12	13	14
Diameter, μm	0.8	0.9	1	3.66	6.1	8.54	11
Mass fraction	0.0114	0.0105	0.0093	0.43	0.29	0.10	0.03

code for the two-phase flow inside the converging and diverging parts of the nozzle up to the nozzle exit.

Step 2: **plume near field.** With the macroparameters at the nozzle exit obtained at Step 1 used as the plume inflow boundary conditions, the computation of the plume near field (first 35 m downstream from the nozzle exit) is performed with a density-based Navier-Stokes solver, CFD++. Since the near field region is the most important part of the flow in terms of particle deflection by plume molecules, the computation has also been performed using a kinetic DSMC-based solver SMILE. The DSMC computations used a starting surface at about 2 m from the nozzle exit plane, with the macroparameters at this surface obtained using CFD++.

Step 3: **plume mid field.** The SMILE solution from Step 2 is used to obtain macroparameters at a new starting surface at 35 m from the nozzle exit. This surface is perpendicular to the plume axis and expands from the nozzle axis to the radial distance of 20 m. The new surface is used as the plume inflow boundary condition for a DSMC computation of the next 300 m from the nozzle exit. The velocities of molecules entering the computational domain from the starting surface were distributed according to the Maxwellian distribution. Again, the SMILE code was used in the DSMC computations.

Step 4: **plume far field.** The last step in the flowfield modeling is the far field computation. The DSMC method is used for this step, and the starting surface obtained from the solution of Step 3 is generated at 250 m downstream from the nozzle exit. The ellipsoidal distribution function[7] is used for molecules entering the domain from the starting surface.

Step 5: **radiation computation**. The UV radiation is calculated using the flow solutions obtained at Steps 2 through 4. A Monte Carlo trajectory based code, NEMO, developed at ERC is used. To compare with experimental data, spectrally resolved and integral radiation was computed along two aft-viewing lines of sight, 4° and 25° from the direction of the plume. The detector is located 1.87 m upstream from the nozzle exit plane, its radial coordinate is assumed to be 0.4 m.

Note that all starting surfaces are located in supersonic flow, with the Mach number typically much larger than unity. This guarantees a negligibly small influence of downstream regions to upstream regions, therefore providing smooth step-to-step transitions. Steps 2 through 4 modeled the interaction of the plume exhaust with the atmosphere. All steps included both gas and particulate phases.

B. Step 1: VIPER solution inside the nozzle

VIPER[8,9] is an axisymmetric Parabolized Navier-Stokes (PNS) code that includes finite rate gas chemistry, multiphase capability (via a two-way coupled Lagrangian method), and a variety of mostly empirical models for gas-particulate interaction and particulate evolution phenomena. The PNS scheme is applied from the
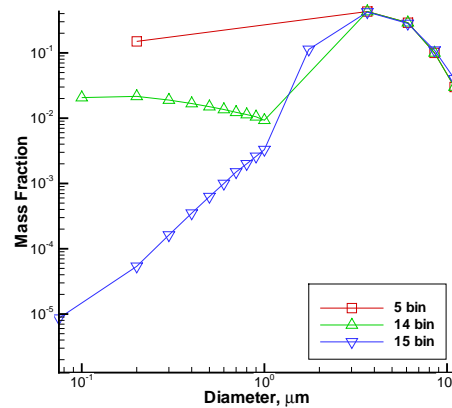
Figure 2. Three particle size distributions.

sonic line near the throat of the nozzle to the exit plane of the nozzle. Separate methods are provided to model the combustion chamber and converging section. The combustion chamber pressure and temperature were assumed to be 34.3 atm and 3450 K, respectively. These conditions result in an exit plane gas pressure of approximately five percent of one atmosphere, which is expected to be well within the region of applicability of this code.

C.   Step 2: CFD++ modeling of plume near field

The flow solver used to perform the near-field simulation is CFD++[10, 11] developed by Metacomp Technologies, Inc. CFD++ is an unstructured, chemically reacting, multi-phase, turbulent, Reynolds Averaged Navier- Stokes (RANS) code. It uses a fully implicit, 2nd order in space, Harten, Lax, van Leer, Contact discontinuity (HLLC) Riemann approximation algorithm, and a modified two equation k-epsilon turbulence model. Finite rate chemistry is used for the simulation of the reactions. An Eulerian based Henderson drag coefficient model[12] is used for the gas-particle flow interactions. A multigrid scheme is used to speed the convergence rate. The simulation assumes that there are pre-computed nozzle inflow conditions defined at the exit plane of the nozzle. These exit plane flow conditions are obtained using the VIPER code.

All the 2D axisymmetric grids used a baseline mesh of approximately 50,000 quadrilateral nodes. For simplicity, the nozzle exit plane is assumed to be flush with the base of the vehicle. Care must be taken such that the initial cell size is significantly resolved to accurately capture the dynamics of the multi-phase flow. Too large of an initial grid spacing will lead to improper particle tracking and ultimately an incorrect particle distribution. From a grid resolution study it was found that an initial grid spacing of 0.001 m was sufficient to preserve accurate particle physics.

Four unique boundary conditions are used for the axisymmetric simulations. The far field has a characteristic based inflow/outflow boundary condition imposed on it. A symmetry plane boundary condition is imposed at the center line. A Knudsen number based slip wall boundary condition is used at the body of the missile. Finally, a prescribed inflow condition is used at the exit plane of the nozzle.

D.   Steps 2, 3 and 4: SMILE simulation of the plume

The axisymmetric capability of the DSMC-based code SMILE[13] was used as the principal kinetic approach. The important features of SMILE that are relevant to this work are parallel capability, different collision and macroparameter grids with manual and automatic adaptations, and spatial weighting for axisymmetric flows. The majorant frequency scheme[14] was used to calculate intermolecular interactions. The intermolecular potential was assumed to be a variable hard sphere.[15] Energy redistribution between the internal and translational modes was performed in accordance with the Larsen-Borgnakke model. Temperature-dependent relaxation numbers were used. Species weights were used for particulate species, different for different steps

American Institute of Aeronautics and Astronautics Paper 2008-4120

and particle diameters. The reflection of molecules on the rocket surface was assumed to be diffuse with complete energy and momentum accommodation.

The total number of simulated molecules and particulates was approximately 19 million for Step 2, 15 million for Step 3, and 10 million for Step 4. The number of collision cells for these cases is 5, 4.5, and 3 million, respectively. Note that an additional calculation has been carried out for Step 3 with 5 million molecules and 1.5 million cells, and no visible difference was observed between that and the first simulation. The location of the hand-off surfaces was set so that the conventional DSMC requirements of the cell size, number of molecules, and time step, are satisfied.

E.   Step 5: radiation prediction with NEMO

A parallel Monte Carlo radiation code, NEMO, developed at ERC, that has 2D and 3D modules and generally allows for prediction of radiation from two-phase rocket plumes in the UV, visible, and IR ranges, was used in this work. To calculate the emissivity of alumina and soot particles, it is necessary to know optical properties of the corresponding materials. The real part of the complex refraction coefficient of alumina particles was calculated using the expression given in Ref. 16. The imaginary part was calculated using two different sets of expressions, (i) set of Ref. 17, and (ii) set of Ref. 18. When calculating the absorption index according to Ref. 18, to provide for a smooth transition between the fundamental absorption and the Urbach edge absorption, a term $b\lambda_{opt}$ was added to the expression for the fundamental absorption, similar to Ref. 17. For soot, the complex refraction index was calculated according to Ref. 20. Once the optical properties of the materials in the temperature and wavelength ranges of interest (300-3,000 K and 0.2-20 μm, respectively) were calculated, the absorption efficiency Q_{abs} was calculated for the given particle radii using the BHMIE code first published in Ref. 19. Then, the particle emissivity ϵ was obtained as

$$\epsilon = \int_{\lambda_{min}}^{\lambda_{max}} Q_{abs}E_{b\lambda}d\lambda / \sigma T^4 \tag{1}$$

where $E_{b\lambda}$ is the black body emissive power, σ is the Stefan-Boltzmann constant, $\lambda_{min} = 0.2$ μm, and $\lambda_{max} = 20$ μm.

The two different sets of expressions result in significant differences in the absorption index for the range of temperatures important in this work, as illustrated in Fig. 3 (left). Note that the newer data set is characterized by much lower absorption index for higher wavelengths, which is expected to strongly impact the UV spectra. The difference is also reflected in particle emissivities computed with these sets. Figure 3 (right) shows emissivities for 0.2 and 3.66μm diameter particles as a function of surface temperature, calculated using Ref. 17 and Ref. 18. As expected, the emissivity is much higher for bigger particles. The temperature dependence is similar for both diameters. For model,[17] the emissivity stays approximately constant until the temperature reaches ~1750 K, and then grows rapidly. For model,[18] the emissivity starts growing after 2000 K. In the 2000-3000 K temperature range, the emissivity predicted by model[17] is much higher than both liquid and γ-phase emissivities predicted by model.[18]

IV.   Results and Discussions

A.   Nozzle Exit Plane

As discussed in the previous section, the first step in the present multi-step approach is to obtain the solution of the two-phase flow inside the nozzle using the VIPER code, and generate a starting surface at the nozzle exit plane for the successive CFD++ modeling. The profiles of the gas and particle properties in the radial direction immediately downstream from the nozzle exit plane are shown in Fig. 4 for the 14-bin distriution (Table 4). The location Y=0 corresponds to the nozzle axis. Gas density has a clear maximum in the boundary layer, and then decreases in the vicinity of the nozzle lip, primarily due to the adiabatic surface model used in VIPER. The sub-micron particles mostly follow the gas due to the large influence of the drag force. Larger particles, though, due to their large inertia, have lower maximum deflection angle than the nozzle half-angle of 15°. Also, there is a smaller impact of the boundary layer and less visible increase in 3.66μm particle density at larger radial locations as compared to the smaller particles. The temperature of 3.66μm particles is close to the alumina melting temperature of 2320 K, and the effect of particle crystallization is evident at Y>0.12 m, where the temperature is constant at 2320 K.
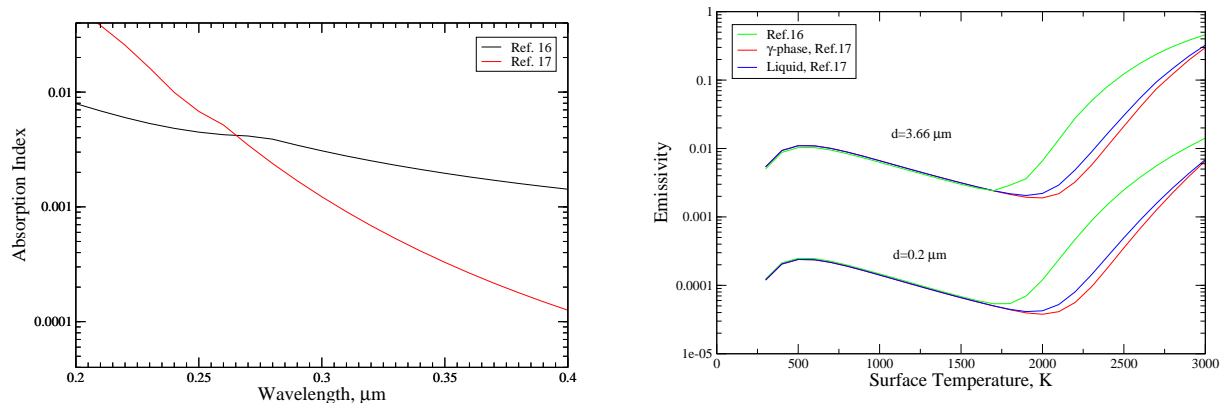
Figure 3. Alumina absorption index calculated with two different sets of expressions, Ref. 17 and Ref. 18 (γ phase), for a surface temperature of 2,200 K (left). Emissivities for two particle diameters computed with these two sets (right).

Gas temperature is half of its stagnation value near the nozzle axis, and decreases closer to the boundary layer. The temperature of the submicron particles is on average over 200 K larger than the gas temperature, but still significantly lower than that of the alumina melting temperature, which indicates that the smaller particles are fully crystallized.

Figure 4. Gas and particulate density (left) and temperature (right) along the nozzle exit.

B. Plume Near Field

The numerical analysis of the plume near field is conducted using both the solution of the Navier-Stokes equations and the DSMC method. To analyze the impact of the alumina particle emissivity and size distribution, four different cases are considered for the flow outside the nozzle,

    (1) 5 bin distribution of alumina particles with emissivities computed using Ref. 17,

    (2) 5 bin distribution of alumina particles with emissivities computed using Ref. 18,

    (3) 14 bin distribution of alumina particles with emissivities computed using Ref. 18,

    (4) 15 bin distribution of alumina particles with emissivities computed using Ref. 18.

    The gas properties in the near field obtained with the two approaches are presented in Fig. 5. Only the results for Case 1 are shown below, since the flowfields for the other cases are similar. The rocket's leading edge is located at X=0. Hereafter, the dark region near the nozzle exit in the DSMC field corresponds to the region not included in the modeling; its outer region shows the starting surface for the the DSMC. There

American Institute of Aeronautics and Astronautics Paper 2008-4120

Distribution A: Approved for public release; distribution unlimited

are two regions with elevated pressures, the first (inner) is due to the plume only beginning to expand, and the second (outer) corresponds to the interaction region between the hypersonic free stream and the plume. There are some difference observed between the continuum and kinetic solutions. First, the structure of the shock wave is different. To understand this difference, one needs to recall that the ambient mean free path at 118 km is 3 m, which corresponds to a Knudsen number of unity based on the rocket length. This results in the formation of a viscous shock layer characterized by a bimodal molecular velocity distribution. The Navier-Stokes equations are not applicable in this case, and are known to significantly underpredict the thickness of the shock front. Second, there is a difference in the plume, with pressures computed with the DSMC method being up to 30% higher than those in the continuum solution. This fact is primarily attributed to the difference in the gas-particle heat transfer models used in SMILE and CFD++ (a detailed analysis of this behavior may be found in Ref. 21). In the absence of any reliable information on the translational and internal energy accommodation of gas molecules on liquid alumina, a complete energy accommodation was used in the DSMC computations, which likely overestimates the actual heat flux from the particles to the gas. The lower gas temperatures result in higher Mach numbers in CFD++, as illustrated in Fig. 5 (right). Note that there is a very small difference the gas density and velocity obtained with the two approaches.
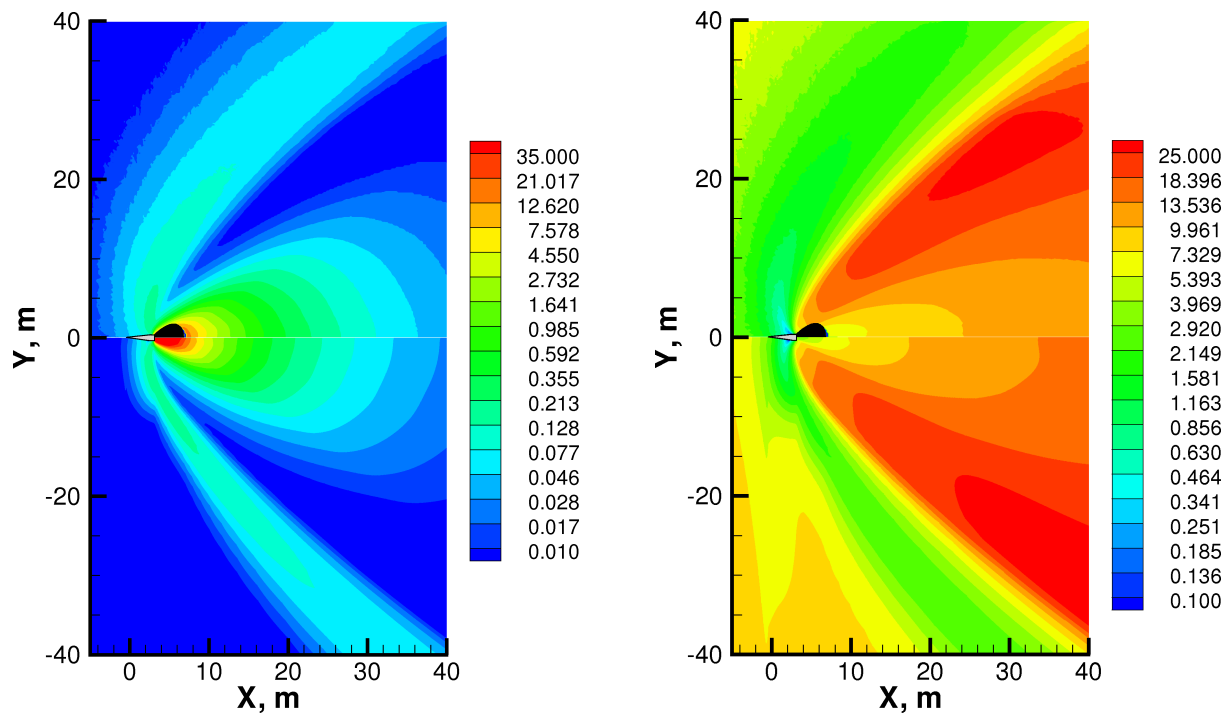

Figure 5. Near field gas pressure in Pa (left) and Mach number (right) computed with SMILE (upper halves) and CFD++ (lower halves).

Similarly, the difference in particle number densities is also very small, as shown in Fig. 6 for 0.2μm diameter alumina particles. The maximum divergence angle for these particles approaches 35°, and a large number of the submicron particles are in the field of view of the far-field (25°) photometer. However, the particle temperature along the 25° line of sight is below 1,000 K, which is not sufficient for these particles to be a direct source of UV radiation. Still, these particles can reflect the photons coming from the hot particles in the core flow.

The agreement between the two numerical approaches is very good both in the core flow and at larger angles from the nozzle axis. The comparison of 0.2μm particle surface temperature shows a visible difference between the two solutions, with DSMC particle temperatures lower in most of the plume. The difference, which approaches 100 K in the core flow, is primarily due to the the gas-particle heat transfer models used in CFD++ and SMILE. Previous studies have shown that the effect of the heat transfer model is larger for 0.2μm particles. Additional DSMC computations, not shown here, demonstrated that the difference is much smaller when the translational and internal energy accommodation coefficients of 0.5, instead of the baseline 1, are used.
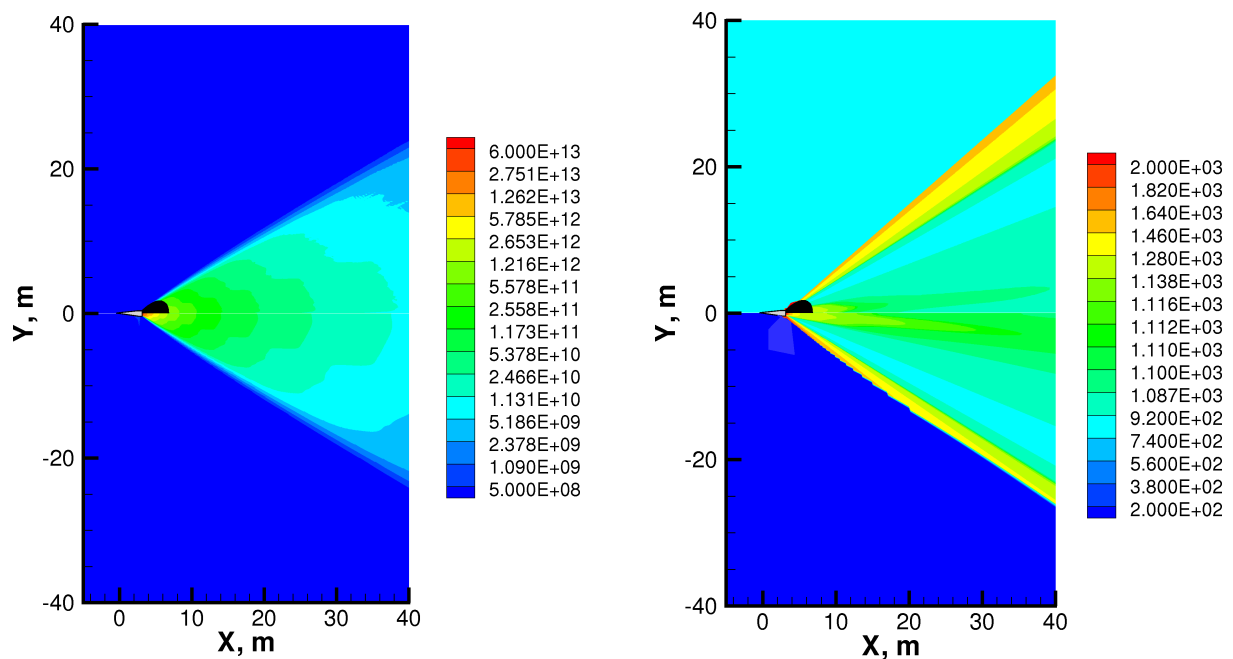
Figure 6. Near field 0.2μm diameter particle number density in particle/m^3 (left) and surface temperature in Kelvin (right) computed with SMILE (upper halves) and CFD++ (lower halves).

Comparison of the number density and temperature fields for large alumina particles is presented in Fig. 7. The results show that the maximum divergence angle is only about 17° for these particles, which is much smaller than the angle of the 25° photometer. No large particles therefore directly contribute to the radiance measured by the far-field 25°; only photons scattered on sub-micron particles in the side flow are measured. There is very small difference between the density fields obtained by the two solvers, which well within the numerical error bar of the solutions. There is a large difference between the solutions for the particle temperatures, though. In the SMILE solution, where the non-equilibrium alumina crystallization model[22] is used, the particle temperature gradually falls to the critical temperature of 2,100 K, after which the crystallization starts. In CFD++, an equilibrium model of alumina crystallization is used, and the particle temperature stays at 2320 K until the particles are fully solidified. Note that the CFD++ solution in the near field was used in the previous work[1] to calculate the near and far field radiance, whereas this work uses the SMILE solution in the near field. The temperature of large particles is extremely important for the prediction of radiation both in the near and far fields of the plume, and modeling of alumina phase change is therefore important to the results of the simulations.

C. Gas Properties in the Far Field

The results of the near-field SMILE computations are used to provide the starting surface conditions for the middle-field computations, that are in turn used for the far-field modeling. The complete flow fields that illustrate gas properties from the nozzle exit to 2.5 km downstream are given in Fig. 8. The translational temperature field clearly shows the increase in temperature in the mixing layer between the plume and the free stream. Note that the 25° line of sight of the far field photometer intersects with the elevated temperature region at about 500 m from the nozzle. The translational temperature in that region is about 1,000 K, which should not have any implications for UV radiation, except for possible evaporation of condensed liquid droplets (that are not accounted for in this work). Typical for plumes expanding in a background gas, the compression region produced by the interaction of the free stream and the plume converges to the nozzle axis at some distance from the nozzle. In this case, this distance is over 1 km, as the Mach number field clearly shows. The Mach number at the nozzle axis reaches its minimum of about 5 at about 1,400 m from the nozzle. The maximum Mach number of about 30 is observed in the expanding plume at X≈600 m.

Although the mean free path in the free stream is large, and the Knudsen number based on the rocket length of 3.1 m is about 1, the flow in the mixing layer, which is hundreds of meters wide and kilometers long,
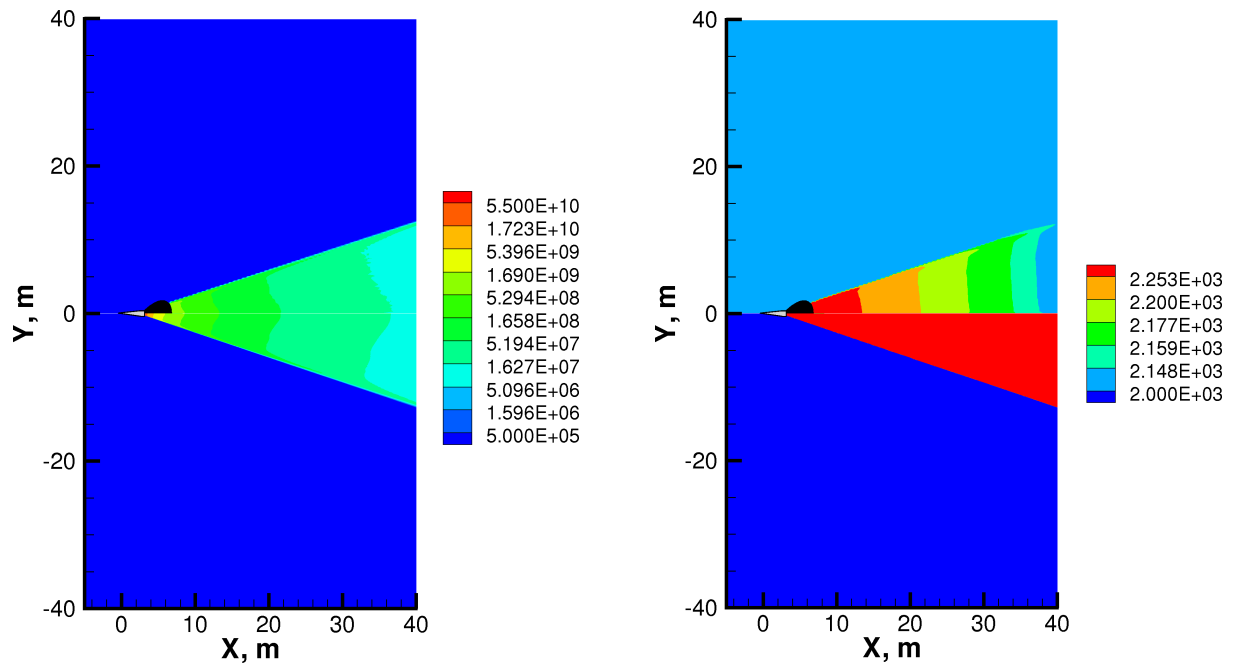
Figure 7. Near field 3.66μm diameter particle number density in particle/m^3 (left) and temperature in Kelvin (right) computed with SMILE (upper halves) and CFD++ (lower halves).

is near-continuum. This is illustrated in Fig. 8 (bottom) where the gas mean free path is plotted. Generally, this makes conventional continuum solvers applicable in that region. However, there is an expansion region in the core flow where the gas mean free path continues to increase, reaching its maximum of about 40 m. The radius of the plume core flow varies from 100 to 200 m, which is comparable to the gas mean free path there. The applicability of continuum approaches in that region may therefore be questionable.

D.   Alumina Particle Properties in the Far Field

Comparison of gas flow fields obtained for different alumina particle emissivities and particle size distributions have shown that the effect of these properties on gas in the far field of the plume is relatively small. The maximum difference observed between Cases 1 and 4 amounted to about 5 percent for gas temperature, and still smaller for gas densities. As expected, the largest effect of particle properties is seen in particle surface temperatures. The comparison of the most important property in terms of UV radiation, namely, the surface temperature of 3.66μm alumina particles, is presented in Fig. 9.

The upper two plots illustrate the impact of the particle emissivity. The values of the emissivity in Case 1 are up to an order of magnitude larger than those in Case 2. This results in much faster cooling of particles. For Case 1, the particle surface temperature decreases to the critical value of 2,100 K at 55 m from the nozzle exit. For Case 2, it takes particles over 400 m to reach this temperature. After the crystallization begins, for both cases the temperature reaches the alumina melting temperature of 2,320 K. This value is reached at about 500 m for Case 2 instead of 60 m for Case 1. One may expect larger effects of the phase change for Case 1 than for Case 2, since particle densities are very small at 500 m. The influence of the size distribution on the particle surface temperature is negligibly small compared to that of particles emissivities for both large and small particles (compare Fig. 9 middle and bottom). Case 4 is practically identical to Case 3, and is not shown here.

Finally, the density of sub-micron particles in the far field is presented in Fig. 10 for Case 2 (the other cases are qualitatively similar). As follows from the near-field results presented above, there is a large number of sub-micron particles in the field of view of the 25° photometer. This, along with high temperature of large particles in the far field, means that the contribution of the far field sub-micron particles on the radiance detected by the 25° instrument may be important and needs to be analyzed. The temperature of these particles does not change much in the far field, and stays at around 1,000 K, which is, again, too low for significant UV emission.
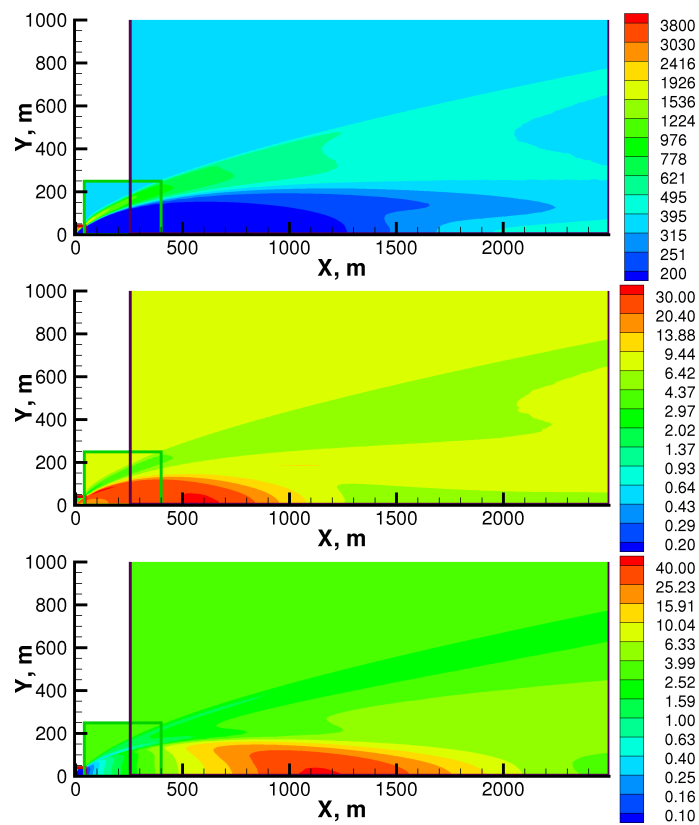
Figure 8. Plume translational temperature in Kelvin (top), Mach number (middle), and gas mean free path in meters.
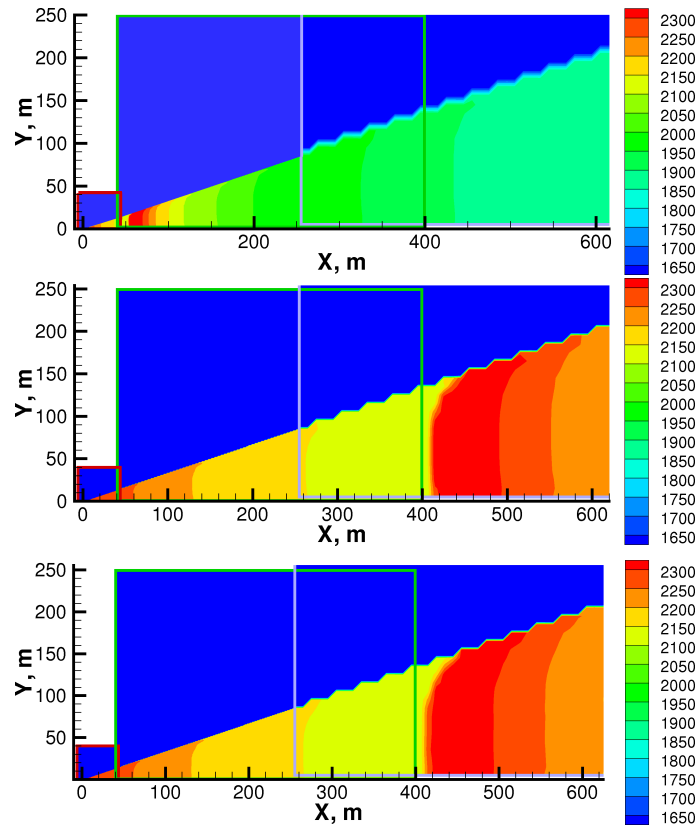
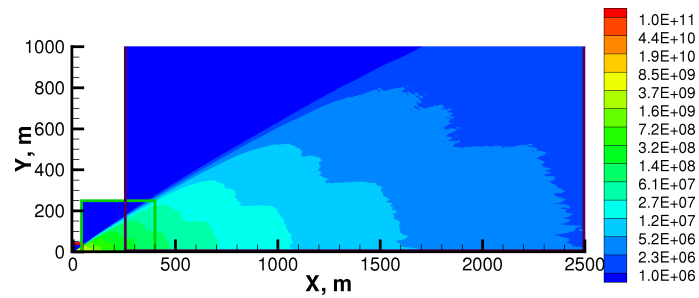Figure 9. Surface temperature field of 3.66μm particles for Case 1, top; Case 2, middle; Case 3, bottom.

Figure 10. Number density field in kg/m^3 of 0.2μm particles.

American Institute of Aeronautics and Astronautics Paper 2008-4120

E.   Soot Particle Properties in the Far Field

The properties of soot in the plume are now examined. Although only Case 1 is shown here, the soot properties for the other three cases are very similar. The number density of 100 nm soot particles is shown in Fig. 11 (left). Similar to sub-micron alumina, a large amount of soot reaches the field of view of the 25° photometer. Light and small soot particles to the large extent follow the gas streamlines in the near field, although then deviate slightly from gas streamlines in the far field. The gas in the far field is too rarefied to significantly affect the soot temperature, although there is a visible increase in temperature at larger angles from the plume axis, where the soot particles interact directly with the free stream. Even though the soot emissivities are much higher than those of same-sized alumina particles, low soot temperatures preclude soot from being direct contributor the the UV emission; only scattering processes are important.
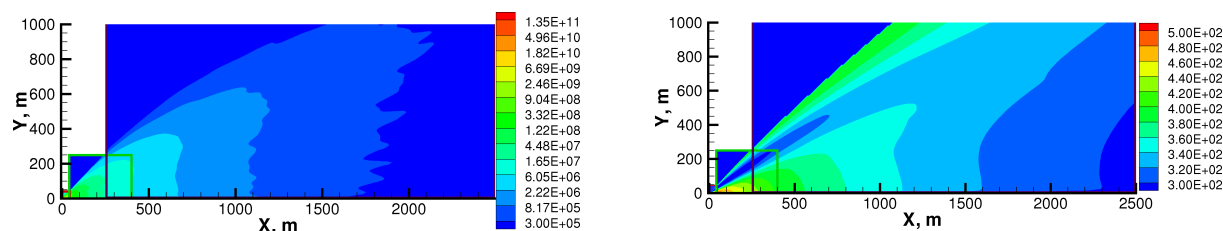

Figure 11. Number density in particle/m³ (left) and surface temperature in Kelvin of 0.1μm diameter soot particles.

The number density profiles of soot particles along the line of sight of the 25° photometer are given in Fig. 12. Very few particles are near the instrument. Note here that the values in the first few centimeters may actually be even lower if soot particles were modeled inside the nozzle, and not just assumed to follow the gas streamlines there. Still, it is believed to be a minor factor in terms of the actual contribution of soot particles in photon scattering, especially keeping in mind the uncertainties in the soot formation and distribution. The soot density reaches its maximum at about 8 m from the detector, and then decreases almost linearly (in log scale) in the far field. There is some deviation from linearity for smaller particles, that is attributed to the impact of the free stream on soot particle trajectories.
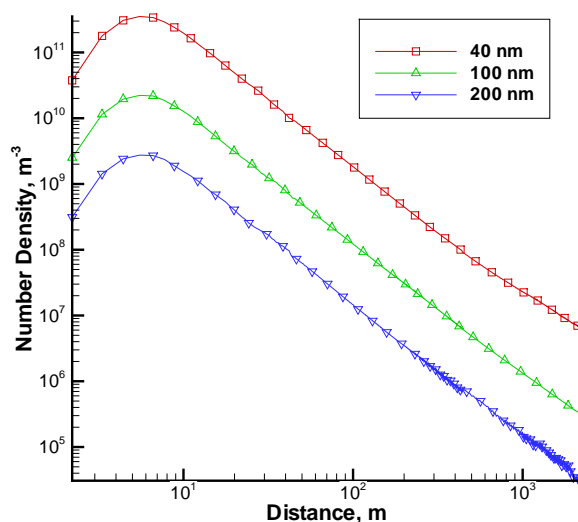

Figure 12. Soot number density along the 25° line of sight.

American Institute of Aeronautics and Astronautics Paper 2008-4120

F. UV Radiance at 4° and 25°

The availability of experimental data[6] allows quantitative analysis of the impact of different factors mentioned above on the radiation intensity. The spectral radiance at 230 nm is presented in Table 5 for four numerical cases under consideration, along with the experimental results.[6] Two photometer lines of sight are considered, 4° and 25°. Consider first the the near field 4° results. A significant decrease in particle emissivities, illustrated in the comparison of Cases 1 and 2, results in an about 20% increase in radiance. This is related primarily to the fact that the temperature of large (micron-sized) particles in the plume decreases much slower for Case 2. The higher temperatures cause more photons to be emitted, even though the emissivities are lower. It is interesting to note that there is a further increase in the radiation when more sub-micron particle bins are included in the computations (compare Cases 2 and 3). The reason for this is photon scattering on small particles. Large number of 0.2μm particles in Case 2 results in significant reduction in radiation due to scattering. When the radiation is computed without sub-micron alumina particle bins, the radiance values for Cases 2 and 3 are almost the same ($8.3 \cdot 10^{-6}$ W/μm m^2 sr for Case 3 against $8.4 \cdot 10^{-6}$ W/μm m^2 sr for Case 2), since the number density and surface temperature of large particles for these two cases are almost identical. The larger number of micron-sized particles and small number of submicron-sized particles result in smaller impact of scattering and the highest radiation for Case 4.

All numerical values for the 4° photometer are noticeably larger than the measured radiation of $3.6 \cdot 10^{-6}$ W/μm m^2 sr. This is primarily attributed to the impact of the gas-particle heat transfer model. Previous analysis[21] have shown that the heat transfer model implemented in CFD++ is reproduced closely by the free molecular model with the energy accommodation coefficients of about 0.4. A model with more efficient heat transfer (larger energy accommodation coefficient) will cool particles inside the nozzle more effectively, and thus the radiative emission would decrease. Another reason is the likely underprediction of the number of sub-micron particles in the numerical simulation, as discussed below.

The result given in Table 5 show that the radiation computed along the 25° line of sight is significantly lower than the measured value. The maximum radiation, recorded for Case 3, is almost three times lower than the data. As all the radiation comes to the 25° detector due to the scattering on sub-micron particles,[1] it is clear that the model underpredicts the amount of these particles in the plume. The formation of somewhat larger number of sub-micron alumina particles is possible, as well as larger soot concentrations in the exhaust. Note also that the current work included only two out of four possible sources of sub-micron particles, aluminum oxidation and soot formation. The other two, heterogeneous- and homogeneous condensation and nozzle surface degradation, are not modeled.

Table 5. Radiation at 230 nm for different models, W/μm m^2 sr. 0.3% soot is included.

Case	4°	25°
Case 1	$4.85 \cdot 10^{-6}$	$3.55 \cdot 10^{-9}$
Case 2	$5.75 \cdot 10^{-6}$	$6.20 \cdot 10^{-9}$
Case 3	$6.99 \cdot 10^{-6}$	$7.70 \cdot 10^{-9}$
Case 4	$9.45 \cdot 10^{-6}$	$2.28 \cdot 10^{-9}$
Experiment	$3.6 \cdot 10^{-6}$	$22 \cdot 10^{-9}$

The impact of soot particles in the plume on the spectral radiation at 230nm is shown in Table 6. The results indicate that the inclusion of 0.3% soot results in a 25% increase in radiation in the far field for Case 2 (the results for Case 3 are similar, whereas for Case 4 the photons reflected on soot particles constitute about two thirds of the total radiation at 25°). It is important to note that all three bins of soot particles (even the smallest bin of 40 nm) contribute noticeably to the far field radiation. The increase of soot mass loading in the plume from 0.3 to 3% results in a drastic increase in the far field radiation, with the 25° line of sight radiation being only about 20% lower than the data (although such a high mass loading of soot does not seem very likely). The near field radiation, that does not change much when 0.3% of soot are considered, decreases about 2% for the 3% soot case.

Relatively large numbers of submicron particles in the far field raise the question of convergence of the obtained results in terms of the length of the computational domain. In order to prove the convergence, the radiation calculations have been conducted with varying domain length (in all runs only the downstream

Table 6. Effect of soot particles on radiation at 230 nm, Case 2.

25°, no soot	$4.83 \cdot 10^{-9}$
25°, 40 nm bin only	$5.21 \cdot 10^{-9}$
25°, 40 nm and 100 nm bins	$5.92 \cdot 10^{-9}$
25°, all soot bins	$6.20 \cdot 10^{-9}$
25°, 3% soot	$1.77 \cdot 10^{-8}$
4°, no soot	$5.75 \cdot 10^{-6}$
4°, 3% soot	$5.62 \cdot 10^{-6}$

boundary was moved). The results for the 25° line of sight are presented in Fig. 13 (left). The main conclusion here is that the radiation shows minumum change after the first few hundred meters downstream from the nozzle axis. Note that the near field radiance converges even faster. That means that the DSMC modeling of the plume near and mid-fields only, without the far field, would provide adequate accuracy for radiation predictions.

Previous results[1] have shown a qualitative difference in the shape of the UV spectra from the published data. While the agreement was reasonable (within a factor of two) for 200-300 nm range, at 400 nm the numerical results overpredicted by a factor of 20. This was attributed mostly to the influence of alumina particle emissivities (the absorption index of Ref. 17 was used in Ref. 1). Similar to the previous results, the computed spectral shape is much steeper than the experimental one when the emissivities based on Ref. 17 are used, as illustrated in Fig. 13, Case 1. The emissivities computed from Ref. 18, however, allow one to capture the shape of the experimental spectra much closer (Cases 2 through 4).
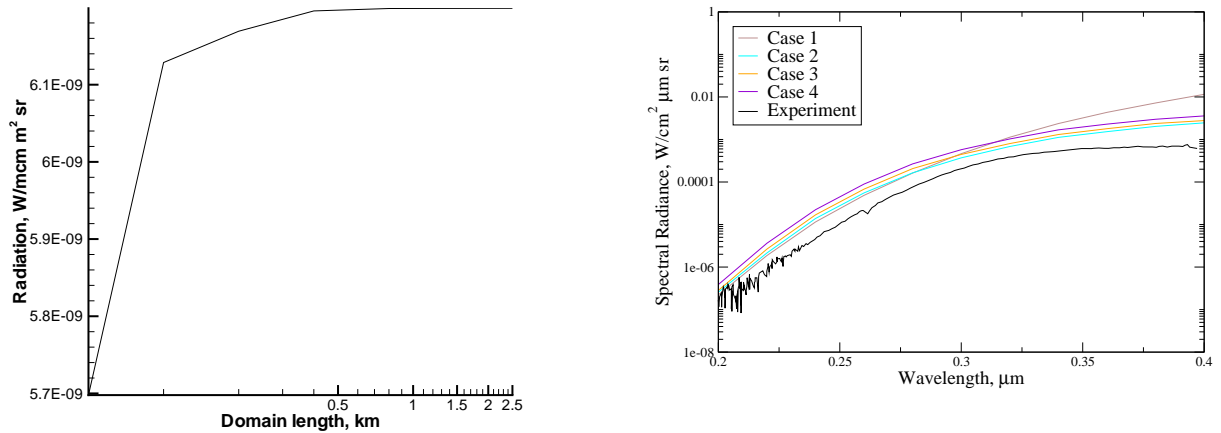

Figure 13. The impact of the far field on the total radiance at 230 nm, Case 2 (left). Comparison of spectral radiance for different cases with experimental data (right).

V. Summary and Conclusions

Computational study of a Star 27 solid propellant rocket plume at an altitude of 118 km has been conducted using a combined multi-step continuum/kinetic approach. The solution of the Navier-Stokes equations was obtained inside the nozzle and in the plume in the vicinity of the nozzle exit. The DSMC method was used to simulate most of the plume, as well as the plume-free stream interaction. A Monte Carlo based radiation solver was used in an overlay mode to calculate UV radiation in the plume. All gas dynamic flow solvers used in this work included two-way coupling between the gas flow and particles, with two types of particles being considered, alumina and soot. Comparison of the continuum and kinetic solutions in the

near field showed some differences in the plume, attributed to different models of gas-particle heat transfer.

The impact of alumina particle emissivities on particle properties and UV radiation in the near and far field has been analyzed. It has been shown that the use of emissivities based on Ref. 18 results in much lower particle temperatures in the plume and significant delay of the liquid-to-γ phase change, as compared to the case when emissivities based on Ref. 17 are used. The radiation was found to be tens of percent higher both in the near and far field when smaller values of emissivities are used due to slower particle cooling. The effect of particle emissivities on the gas is relatively small. Comparison with available experimental data have shown that the model overpredicts the experimental data in the near field ($4°$ line of sight) by on average a factor of two, which is thought to be the effect of the gas-particle heat transfer model inside the nozzle.

The numerical results for the far field ($25°$ line of sight) UV radiation underpredict the measurements, with the difference ranging from almost a factor of ten to about 25%, depending on the sub-micron alumina particle size distribution and soot mass loading. Both these factors are not well known, and were therefore parameterized. Hot micron-sized particle emision in the plume core flow scattered on sub-micron particles in the side flow is the dominant source of the far field UV radiation, and both the alumina particles and soot were found to significantly contribute to the scattering process. It is however expected that other sub-micron particle sources, such as condensation, both heterogeneous and homogeneous, and nozzle erosion, may play a role in UV photon scattering in the far field.

VI. Acknowledgements

References

[1]Gimelshein, N., Lyons, R., Reuster, J., Gimelshein, S., Numerical prediction of UV radiation from two-phase plumes at high altitudes, AIAA Paper 2007-1014, to appear in AIAA Journal.

[2]Erdman, P.W., Zipf, E.C., Espy, P., Howlett, C., Collins, R.J., Cristou, C., Levin, D.A., and Candler, G.V. In-situ measurements of UV and VUV radiation from a rocket plume and re-entry bow-shock, *AIAA Paper 91-0124*.

[3]Schmid, O., Reeves, J., Wilson, J., Wiedinmyer, C., Brock, C., Toohey, D., Availlone, L., Gates, A., and Ross, M., Size-Resolved particle emission indices in the stratospheric plume of an Athena II rocket, JGR, Vol. 108, 4250, 2003.

[4]Reed., R., and Calia, V., Review of Aluminum Oxide Rocket Exhaust Particles, AIAA Paper 93-2819.

[5]Lyons, R., Wormhoudt, J., and Kolb, C. Calculation of visible radiation from missile plumes, AIAA Paper 81-1111, 1981.

[6]Smathers, H.W., Horan, D.M., Cardon, J.D., Malaret, E.R., Singh, M., Sorensen, T., Laufer, P.M., Corson, M.R., Brandenburg, J.E., McKay, J.A., Strunce, R.R. Ultraviolet Plume Instrument Imaging from the LACE Satellite Strypi Rocket Plume, Naval Research Laboratory Report NRL/FR/8121-93-9526, Washington, DC, September 1993.

[7]Cercignani, C., Rarefied gas dynamics: from basic concepts to actual calculations, Cambridge University Press, 2000.

[8]Simmons, F.S. Rocket Exhaust Plume Phenomenology, The Aerospace Corporation Aerospace Press Series, Published by AIAA, 2000, 286p.

[9]Kawasaki, A. H., Coats, D. E., Berker, D. R., A Two-Phase, Two-Dimensional, Reacting Parabolized Navier-Stokes Solver for the Prediction of Solid Rocket Motor Flowfields, AIAA Paper 92-3600.

[10]Chakravarthy, S., and Peroomian, O., Some Internal Flow Applications of a Unified-Grid CFD Methodology, AIAA 96-2926, 32nd AIAA /ASME /SAE /ASEE Joint Propulsion Conference and Exhibit, Lake Buena Vista, FL, July 1996.

[11]Peroomian, O., Chakravarthy, S., and Golberg, U., A "Grid Transparent" Methodology for CFD, AIAA Paper 97-0724.

[12]Henderson, C.A., Drag Coefficients of Spheres in Continuum and Rarefied Flows, AIAA Journal, Vol. 14, No. 6, June 1976, pp. 707-708.

[13]Ivanov , M.S., Markelov, G.N., and Gimelshein S.F. Statistical simulation of reactive rarefied flows: numerical approach and applications, AIAA Paper 98-2669.

[14]Ivanov, M.S., Rogasinsky, S.V., Analysis of the numerical techniques of the direct simulation Monte Carlo method in the rarefied gas dynamics, *Soviet J. Numer. Anal. Math. Modeling*, Vol. 3, No. 6, 1988, pp. 453-465.

[15]Bird, G.A., *Molecular Gas Dynamics and the Direct Simulation of Gas Flows.* Clarendon Press, Oxford. 458 pp, 1994.

[16]Dombrovsky, L.A. Radiation heat transfer in disperse systems. New York: Begell House; 1996.

[17]Anfimov, N.A, Karabadzhak, G.F, Khmelinin, B.A, Plastinin, Y.A, Rodionov, A.V. Analysis of mechanisms and nature of radiation from aluminum oxide in different phase states in solid rocket exhaust plumes, AIAA Paper 93-2818.

[18]Plastinin, Yu., Karabdzhak, G., Khmelinin, B., Baula, G., and Rodionov, A. Ultraviolet, visible and infrared spectra modeling for solid and liquid-fuel rocket exhausts, AIAA Paper 2001-0660.

[19]Bohren, C.F., Huffman, D.R. Absorption and Scattering of Light by Small Particles (Wiley, New York, 1982), Appendix A.

[20]Lee, S.C., Tien, C.L., Optical constants of soot in hydrocarbon flames, Eighteenth Symp.(Int.) Combust.[Proc.], The Combustion Institute, 1981.

[21]Gimelshein, S., Markelov, G., and Muylaert, J. Numerical Modeling of Low Thrust Solid Propellant Nozzles at High Altitudes, AIAA-2006-3273, 37th AIAA Plasmadynamics and Lasers Conference, San Francisco, California, June 5-8, 2006.

[22]Rodionov, A.V., Plastinin, Yu.A., Drakes, J.A., Simmons, M.S., Hiers, R.S., Modeling of multi-phase alumina-loaded jet flow fields, AIAA Paper 98-3462.

American Institute of Aeronautics and Astronautics Paper 2008-4120